

# Implications of Real-Gas Behavior on Refractive Index Calculations for Optical Diagnostics of Fuel-Air Mixing at High Pressures

C. Taber Wanstall<sup>b</sup>, Ajay K. Agrawal<sup>b,a</sup>, Joshua A. Bittle<sup>b</sup>

<sup>a</sup> *corresponding author, [aagrawal@eng.ua.edu](mailto:aagrawal@eng.ua.edu)*

<sup>b</sup> *University of Alabama, Alabama, United States*

---

## Abstract

Three models to compute the refractive index of gaseous mixtures at real gas conditions are presented with the purpose to improve the accuracy of state relationships between refractive index and thermodynamic properties. Models are compared with experimental data to determine one that is applicable to high pressure mixtures with non-ideal thermodynamic behavior near or above a fluids' critical point. The optimal model is applied to analyze adiabatic thermal mixing of fuel and air at typical diesel engine conditions. Results show that the ideal gas mixture law is appropriate in the vapor region, assuming it is known, for example, from experimental measurements. Finally, the model is applied for binary fuel-air mixing at supercritical conditions to demonstrate its full potential.

*Keywords:* Refractivity, Real-Mixture Thermodynamics, Lorentz-Lorenz Equation, Compression Ignition Engine, Polarizability

---

## 1. Introduction

For combustion applications such as diesel engines and gas turbines, fuel is injected into a hot, high pressure oxidizer environment. Ambient air entrainment and turbulent mixing with fuel results in a gaseous phase fuel-air mixing region containing the combustible mixture. Rayleigh scattering can be used to acquire vapor-phase fuel concentration and temperature measurements [1, 2]. In two-phase systems, the Rayleigh scattering signal of the vapor phase must be separated from the Mie scattering signal of the liquid phase. Thus, Mie and Rayleigh scattering diagnostics are often used together, though not simultaneously, to distinguish each phase [3]. Rayleigh scattering is the elastic scattering of light quanta from particles smaller than the wavelength of light, and the measured intensity of the Rayleigh signal ( $I_R$ ) can be related to the local gaseous mixture properties using Eq. 1 [1].

$$I_R = CI_lN \sum_i X_i\sigma_i \quad (1)$$

Where  $C$ ,  $I_l$ ,  $N$ ,  $X$ , and  $\sigma$  are respectively the calibration constant, intensity of the incident light, total number density (molecules per  $m^3$ ), mole fraction, and Rayleigh scattering cross section. The subscript  $i$  represents a species in the gaseous mixture. The Rayleigh scattering cross section is related to the incident light wavelength ( $\lambda$ ) and the species refractive index ( $n$ ) according to Eq. 2 [4].

$$\sigma_i = \frac{24\pi^3}{\lambda^4} \left[ \frac{n^2 - 1}{(n^2 + 2)N_0} \right]^2 = \frac{24\pi^3}{\lambda^4} \left[ \frac{r_e}{N_0} \right]^2 \quad (2)$$

Where  $N_0$  is the total molecular number density at standard pressure and temperature (STP), and the refractivity ( $r_e$ ) is substituted for the refractive

index terms. In the engine community for  $n \approx 1$ , the refractivity ( $r_e$ ) in Eq. 2 is approximated by Eq. 3:

$$r_e = \frac{n^2 - 1}{(n^2 + 2)} \approx \frac{2}{3}(n - 1) \quad (3)$$

thereby approximating the Rayleigh cross-section as Eq. 4 [1].

$$\sigma_i = \frac{24\pi^3}{\lambda^4} \left[ \frac{2(n_i - 1)}{3N_0} \right]^2 \quad (4)$$

For an ideal gas, the number density,  $N$ , is determined from the total inlet enthalpy by assuming adiabatic fuel-air mixing [1, 5] as outlined in the ECN [6]. Relating Rayleigh signal to species mole fraction using Eq. 1 and Eq. 4 requires relationships between the refractive index and the thermodynamic properties (i.e., state relationships) for each species as inputs.

In recent years, the line-of-sight rainbow schlieren deflectometry (RSD) technique has been used to obtain the thermodynamic properties in laminar gaseous systems, as outlined in Ref. [7]. However, Wanstall *et al.* have shown the potential of RSD for quantitative measurements in the fuel-air mixing region of diesel sprays [8]. They developed the RSD methodology to simultaneously detect the liquid phase boundary and estimate thermodynamic properties in the surrounding vapor zone to overcome the need for requiring two separate diagnostics for such measurements [8, 9]. RSD directly measures the refractive index which can be related to the thermodynamic properties using the state relationships discussed previously. For an ideal gas with  $n \approx 1$ , refractive index is related to density using the Dale-Gladstone equation:

$$n - 1 = k\rho = k \frac{PM}{RT} \quad (5)$$

Where  $k$  is the Dale-Gladstone constant,  $P$  is the pressure,  $M$  is the molecular weight,  $\bar{R}$  is the universal gas constant, and  $T$  is the temperature. For an ideal gas mixture,

$$n - 1 = k_{mix}\rho_{mix} = \frac{P}{RT} \sum k_i M_i X_i \quad (6)$$

where  $X_i$  is the species mole fraction, and subscript  $i$  refers to species  $i$ . The Dale-Gladstone relation uses the same linearized approximation for refractive index ( $n \approx 1$ ) shown in Eq. 3. Thus, both Rayleigh scattering and RSD rely upon the state relationships between refractive index (only the real-part is considered here) and thermodynamic properties, e.g., Eq. 5 for an ideal gas and Eq. 6 for ideal gas mixtures.

Both Rayleigh scattering and RSD have been used to obtain accurate measurements in combustion environments at atmospheric pressures [10, 11]. However, state-of-the-art combustion engines operate at high pressures (e.g., cylinder pressures exceeding 100 bar in diesel engines) and thus ideal gas law and/or ideal mixing laws (e.g., Amagat's Law) may not be applicable.. Recent experimental and theoretical findings have challenged the conventional paradigm by suggesting that the pressure and temperature in modern diesel engines can exceed the thermodynamic supercritical conditions for liquid/gas mixtures in regions of the fuel jet [12, 13, 14, 15, 16, 17, 18, 19]. Thus, the mixing processes and mixture laws in fuel spray could be different than conventionally described. [20, 21]. Oefelein *et al.* have described the evolution of a purely supercritical spray without liquid droplets and surface tension forces where mixing between the fuel jet and the surrounding ambient is dominated by turbulent diffusion [22]. These non-ideal gas conditions require real fluid thermodynamic mixture models. Large eddy simulations

(LES) studies based on real fluid equation of state (EOS) have determined that the fuel-air mixing is profoundly modified by the non-ideal gas thermodynamic properties [23, 24, 25]. Recently, Crua *et al.* showed that the fuel-air mixing at diesel conditions can occur by the classical evaporation of fuel droplets, purely diffusive mixing between supercritical fuel and ambient air, or a combination of both, i.e., transcritical mixing, depending on the pressure and temperature of the ambient environment [18].

The above review raises the following important question, “Are current ideal gas mixture laws relating refractive index to thermodynamic properties valid for applications such as modern diesel environments where the gaseous mixtures can be non-ideal?”. Thus, the objective of this study is to develop a robust model to relate optical (e.g, refractive index) and thermodynamic (e.g., density) properties of real-gas mixtures at high pressures. This paper is divided into six more sections. First, the Lorentz-Lorenz equation providing the link between a microscopic quantity (polarizability) and a macroscopic quantity (refractive index) is presented. The next two sections discuss polarizability and thermodynamic models for pure substances and gaseous mixtures. Then, three different models are presented to compute the refractive index of a real gas mixture, and compare them against experimental data available in the literature. Next, the refractive index models are investigated for an extensive range of diesel engine conditions including Spray A, as defined by the ECN community [6]. Then the best model is applied to the problem of fluid mixing at supercritical conditions to demonstrate its full potential. Finally, the conclusions of the paper are summarized.

## 2. Lorentz-Lorenz Equation

The theoretical basis for relating refractive index to density is embedded in the state equation of electromagnetic polarization established in the late 19<sup>th</sup> and early 20<sup>th</sup> century [26, 27]. As the electromagnetic wave travels through a medium, the wave’s phase velocity changes proportionally to the refractive index of the substance. At the atomic level, this is caused from disturbances created by the electromagnetic field in the charge of each atom (mostly electrons), and how closely the charges are packed (density). The susceptibility of the substance to these disturbances is called the molecular polarizability,  $\alpha$ . The end result is the so called Lorentz-Lorenz equation relating refractive index to molecular polarizability ( $\alpha$ ) and molar density ( $\bar{\rho}$ ) shown in Eq. 7 from which the Dale-Gladstone equation (Eq. 5) is derived. The Lorentz-Lorenz equation applies to an isotropic system containing non-polar substances with no molecular interactions, e.g., each molecule is treated as an isolated system.

$$r_e = \frac{n^2 - 1}{(n^2 + 2)} = \frac{N_A \alpha}{3} \bar{\rho} = \frac{N_A \alpha}{3M} \rho \quad (7)$$

Where  $N_A$ ,  $\alpha$ , and  $M$  are Avogadro’s number (constant), mean molecular polarizability, and molecular weight, respectively. Note that Eq. 7 can be written either using molar or mass density ( $\rho$ ). For  $n \approx 1$ , the Lorentz-Lorenz equation (Eq. 7) can be simplified to the Dale-Gladstone formulation (Eq. 5) in which the Dale-Gladstone constant is:

$$\kappa = \frac{3 N_A \alpha}{2 3M} \quad (8)$$

Figure 1 plots the error in refractivity  $r_e$  introduced by the Dale-Gladstone approximation for various hydrocarbons, and highlights regions with errors

greater than 5 and 10 percent. The exponential of  $r_e$  is shown on the vertical axis to highlight the difference between Lorentz-Lorenz and Dale-Gladstone equations. Considering the error introduced by the Dale-Gladstone approximation, especially at high refractive index values, it is not recommended for the analysis. The Lorentz-Lorenz Eq. 7 requires virtually no additional effort with today's modern computing power. Thus, moving forward, the Lorentz-Lorenz Eq. 7 will be used and the Dale-Gladstone Eq. 5 will not be considered.

The primary focus of the present study is to extend Eq. 7 for gaseous mixtures at high pressures. This requires accurate models to relate the mixture refractivity (or mixture refractive index) to polarizability and density of the mixture and/or its components. In the next two sections, polarizability and density calculations for pure substances and mixtures are discussed, and then, different refractivity mixture models analyzed in this work will be introduced.

### 3. Polarizability Models

#### 3.1. Single Component

Polarizability is often reported in the literature at standard temperature and pressure (STP),  $T = 273$  K and  $P = 1$  bar. Gardiner *et al.* provide a detailed data set for polarizability of numerous combustion related substances in [28], and Bosque *et al.* provide one of the largest experimental data sets for polarizability with over 400 compounds including many diesel surrogate fuels [29] such as *n*-heptane and *n*-dodecane. However, the validity of using polarizability data at STP for applications at high pressures or temperatures

is not immediately clear. Thus, existing literature was searched to identify experimental studies that report polarizability of several gases as functions of pressure and temperature [30, 31, 32]. Figure 2 shows the percent change in polarizability with pressure for seven species relevant to this study at a constant temperature of 305 K except for heptane at 550 K, i.e., close to its critical temperature.

Figure 2 shows a slight increase and then decrease in polarizability with increasing pressure for all seven species. However, the change in polarizability with pressure is small, less than 1 percent, except for  $CO_2$  at around its critical point of 304 K and 73.9 bar where the difference from the STP value is about 4.5%. Polarizability also has a slight linear temperature dependence [32], especially for propane among the seven species considered in this study. However, at some pressures/temperatures the temperature effect counteracts the pressure effect, e.g., the temperature effect can cause a decrease in polarizability while the pressure can cause an increase [32]. Still, the effect of pressure and temperature on polarizability is quite small for combustion relevant species, less than 5% of the value at the reference conditions. Thus, following the Lorentz-Lorenz formulation of Eq. 7, polarizability at STP is used to rewrite Eq. 7 as Eq. 9

$$r_e = \frac{n^2 - 1}{n^2 + 2} = \bar{A}\bar{\rho} = A\rho \quad (9)$$

where  $\bar{A} = \frac{N_A\alpha}{3}$  and  $A = \frac{N_A\alpha}{3M}$  are, respectively, mole and mass based constants. More advanced forms of the Lorentz-Lorenz Eq. 7 have been developed by Buckingham [33, 34, 35] where the refractivity (or refractive index) is calculated from a higher order virial expansion as shown in Eq. 10. Equation 10 accounts for pressure and temperature effects on polarizability as

shown in Fig. 2.

$$r_e = \frac{n^2 - 1}{n^2 + 2} = [\bar{A} + \bar{B}\bar{\rho} + \bar{C}\bar{\rho}^2 + \dots]\bar{\rho} \quad (10)$$

### 3.2. Mixtures

For mixtures, Buckingham *et al.* [36] derived a theoretical basis for Eq. 10 as shown in Eq. 11.

$$\bar{A}_{mix} = \sum_i \bar{A}_i X_i \quad (11a)$$

$$\bar{B}_{mix} = \sum_{i,j} \bar{B}_{i,j} X_i X_j \quad (11b)$$

The constant  $\bar{A}$  is the same as in Eq. 9. However, the coefficient  $\bar{B}$  requires an interaction term ( $B_{ij}$ ) which is generally unknown. Since the higher order virial coefficients are negligible (as shown in the last section), the first term alone (i.e.,  $\bar{A}$ ) is a good approximation to compute the mixture polarizability, and will be used in this study. Nearly linear behavior of mixture polarizability ( $\bar{A}_{mix} = \sum_i \bar{A}_i X_i$ ) has been observed in supercritical environments for methanol-carbon dioxide and ethanol-carbon dioxide mixtures [37, 38].

## 4. Thermodynamic Models

### 4.1. Single Component

Real fluid EOS are well-developed for determining thermodynamic properties at non-ideal gas conditions. The most useful EOS are semi-empirical or empirical in nature. Once reasonable computing power became available in 1960s, empirical multiparameter EOS became the new standard [39].

The most recent and accurate multiparameter EOS are formulated in terms of reduced Helmholtz energy,  $a$ . Equation 12 shows the form of the reduced Helmholtz EOS [40]

$$\begin{aligned}\frac{a(T, \rho)}{RT} &= \frac{a^{IG}(T, \rho) + a^R(T, \rho)}{RT} \\ &= f^{IG}(\tau, \delta) + f^R(\tau, \delta).\end{aligned}\quad (12)$$

where  $T$  is temperature,  $R$  is the ideal gas constant, the parameters  $\delta$  and  $\tau$  are the reduced density and temperature based on the critical values ( $\rho/\rho_c$  and  $T_c/T$ ). The superscripts IG and R stand for the ideal gas and residual, respectively. The ideal gas Helmholtz energy is generally obtained from the isobaric ideal gas heat capacity correlation shown in Eq. 13

$$\begin{aligned}a^{IG} &= a_o + \int_{T_o}^T (c_P^{IG} - R)dT - \\ &T \int_{T_o}^T \frac{c_P^{IG} - R}{T} dT + RT \ln\left(\frac{\rho}{\rho_o}\right).\end{aligned}\quad (13)$$

where  $c_p$  is the specific heat and the subscript  $o$  refers to a chosen reference state. Often empirical calorimetric data ( $c_p$ ) are correlated with polynomial functions [40].

The residual part, loosely supported by theoretical considerations, is given by a general empirical function:

$$f^R(\tau, \delta) = \sum_{k=1}^{k=n} N_k \delta^{d_k} \tau^{t_k} + N_k \delta^{d_k} \tau^{t_k} \exp(-\delta^{l_k}). \quad (14)$$

Where  $N$ ,  $d$ ,  $t$ , and  $l$  are substance specific coefficients determined by a complex multivariable fitting procedure; in which the summation contains between 4-20 terms [41]. Often vapor-liquid equilibrium of a substance is utilized to optimize these EOS parameters. Once the EOS is determined,

consistency can be checked by ensuring that pressure (P), temperature (T), and Gibbs function ( $\bar{g}$ ) values follow vapor-liquid ( $V$  and  $L$ ) equilibrium conditions, respectively.

$$\begin{aligned} P^L &= P^V \\ T^L &= T^V \\ \bar{g}^L &= \bar{g}^V. \end{aligned} \tag{15}$$

Figure 3 shows the effect of pressure on density in terms of percent difference between real gas and ideal gas models. Figure 3 shows that computing density from ideal gas law leads to large errors at high pressures, as expected. The sharp peaks for methane, heptane, and carbon dioxide in Fig. 3 are a consequence of phase change not accounted for by the ideal gas law. At temperatures farther away (higher) from the critical point, the errors would decrease because the density decreases at high temperatures (for a given pressure), and hence, the substance approaches towards the ideal gas conditions, i.e., compressibility factor closer to unity. Comparing Fig. 2 and Fig. 3, one can observe that the pressure has a negligible effect on polarizability but a much greater effect on the density of the pure substance. Thus, accurate density calculations will require a real gas equation of state at high pressures.

#### 4.2. Mixtures

The Helmholtz energy equation can be extended to fluid mixtures. Each component of the mixture is linearly combined and weighted by mole fraction to obtain the mixture EOS. For fluid mixtures with negligible intermolecular interactions between the species, mole weighted additive principle is sufficient. However, a comprehensive treatment of fluid mixtures requires a

departure function to account for the intermolecular mixture dynamics. The departure function is determined through regression analysis of available experimental data [42, 43] and is shown in Eq. 16 where  $\vec{X}$  represents the mole fraction of all species as a vector.

$$f(\tau, \delta, \vec{X}) = \sum_i X_i f_i^{IG}(\tau, \delta) + X_i f_i^R(\tau, \delta) + \Delta f(\tau, \delta, \vec{X}) \quad (16)$$

This approach was further improved for binary mixtures in Ref. [44] where the reducing functions,  $\tau(x)$  and  $\delta(x)$ , are determined for the mixture to produce a reduced mixture Helmholtz EOS. The mixture's reduced temperature and density are determined by applying weighting functions to each component's reduced temperature and density and the general functional form is shown in Eq. 17

$$Y_r(\mathbf{X}) = \sum_{i=1}^N x_i^2 Y_{c,i} + \sum_{i=1}^{N-1} \sum_{j=i+1}^N 2x_i x_j \frac{x_i + x_j}{\beta_{Y,ij} x_i + x_j} Y_{ij}. \quad (17)$$

Where  $Y$  is a function of either density or temperature,  $\beta$  is one of the fitting parameters, and the subscripts r and c refer to the reduced and critical property parameters, respectively. The fitting parameters e.g.  $\beta$  in Eq. 17 are obtained by matching the numerical thermodynamic surface to experimental data points for the mixture, namely the bubble and dew points. The binary interaction parameters, and thus, the mixture EOS obtained are only as good as the experimental data upon which they are based [44]. In this study, the software package REFPROP by NIST incorporating the above methodology with features such as a python library for thermodynamic mixture property calculations [45] for a limited number of substances and even a smaller set of binary mixtures has been used.

## 5. Refractive Index Models

### 5.1. Model Development

The Lorentz-Lorenz Eq. 7 was formulated for pure substances, and unfortunately, little research exists to extend it to real gas mixture at high pressures. Nevertheless, Liu et al. provide a detailed summary of different first order mixture laws for refractivity ( $r_e$ ) neglecting the higher order terms in Eq. 10 and the subtleties associated with each one [46]. Mixture laws can be divided into two categories - additive refractivity and additive polarizability. Both are an extension of the Amagat's law whereby the mixture property is calculated as the mole-weighted summation of the component property, i.e., refractivity or polarizability. The general form of the additive refractivity formulation is given in Eq. 18.

$$r_{e,mix} = \sum_i r_{e,i} X_i = \sum_i \bar{A}_i \bar{\rho}_i X_i \quad (18)$$

In the additive polarizability formulation, the mixture polarizability,  $\bar{A}_{mix}$ , is calculated from Eq. 11a to obtain the mixture refractivity,  $r_{e,mix}$ , from Eq. 19.

$$r_{e,mix} = \bar{\rho}_{mix} \bar{A}_{mix} = \bar{\rho}_{mix} \sum_i \bar{A}_i X_i \quad (19)$$

Here,  $\bar{\rho}_{mix}$  is the mixture density. These formulations have been used for mixtures of gases and liquids, though with no particular attention to real gas mixtures. In this study, three different models are formulated to calculate the refractivity of gaseous mixture. The first is an ideal gas model while the last two are real-gas models. For the ideal gas model, the two formulations in Eq. 18 and Eq. 19 are identical.

*Ideal Gas (IG) Model*

$$\frac{n^2 - 1}{n^2 + 2} = \sum_i \bar{A}_i \bar{\rho}_{i,IG} X_i = \bar{\rho}_{IG,mix} \sum_i \bar{A}_i X_i \quad (20a)$$

*Real Gas Model 1 - Additive Refractivity (AR)*

$$\frac{n^2 - 1}{n^2 + 2} = \sum_i \bar{A}_i \bar{\rho}_{i,RG} X_i \quad (20b)$$

*Real Gas Model 2 - Additive Polarizability (AP)*

$$\frac{n^2 - 1}{n^2 + 2} = \bar{\rho}_{mix,RG} \sum_i \bar{A}_i X_i \quad (20c)$$

In this work, Eqs. 20a-c are referred to as the IG, AR, and AP models, respectively. Note that additive refractivity and additive polarizability formulations are different for real gas mixtures. The AR model uses species polarizability at STP and the density of each species is computed from real-fluid EOS as discussed in Section 4.1. For AP model, the mixture polarizability is mole-weighted sum of species polarizability at STP, and the mixture density is obtained from real-fluid mixture EOS as discussed in Section 4.2.

## 5.2. Model Validation

The above mixture models are compared against experimental refractive index data at high pressures relevant to compression ignition engines. Unfortunately, very limited experimental data exist [37, 38, 47, 48, 49] of which [49] provides the most extensive measurements of refractive index of mixtures for a large range of high pressures. Thus, Ref. [49] will be used to compare the three refractive index mixture models presented above.

In Ref. [49], the refractive index was measured by a Michelson interferometer with a maximum relative uncertainty of 0.03%. The refractive index

was measured for binary mixtures of methane and carbon dioxide at pressures ranging from 0.5 to 20 MPa, and a fixed temperature of 303 K. Six different mole fractions of  $CO_2$  were studied: 0%, 50%, 78.2%, 80.2%, 82.2%, and 100%. In our study, the molar polarizability for methane and carbon dioxide is taken from [28]. For each test condition in Ref. [49], the density is calculated by the ideal gas law for the IG model, reduced Helmholtz EOS for each component for the AR model, and reduced Helmholtz EOS for the mixture for the AP model.

Figure 4 shows the computed refractive index difference ( $n-1$ ) for each model compared with experimental data for a binary mixture of 78.2%  $CO_2$  and 21.8%  $CH_4$  at pressures of 1 to 200 bar. For pressures below about 30 bar, all models predict nearly the same linear increase in the refractive index difference with an increase in the pressure. In this regime, the mixture behaves as an ideal gas, thus, the IG model is a valid approximation. Additionally, the AR and AP models are equivalent, and same as the IG model, indicating that each species also behaves as an ideal gas. However, at pressures above 30 bar, the refractive index difference is increasingly under-predicted by the IG model.

The two real gas models provide very different results at pressures above 50 bar: AR model grossly overpredicts while AP model shows excellent agreement with experimental data for the entire pressure range. At high pressures, the compressibility (or real-gas behavior) affects the density significantly but polarizability is nearly constant as shown in Figs. 2 and Fig. 3. However, the AR model combines both density and polarizability as one "lumped" parameter weighted linearly with the mole fraction. The net effect is a higher

(and erroneous) weighting for components with higher density. The non-linear behavior of density is most significant near the critical point and phase boundaries. The experimental data in Fig. 4 were obtained at 300 K. The density of carbon dioxide will exhibit highly non-linear behavior near its critical point of 304.4 K and 73.8 bar, which explains the large errors introduced by the AR model at around 70 bar. The error decreases at higher pressures as conditions depart away from the critical point. Note that the test conditions are far above the critical point of methane (190 K and 46.5 bar), i.e., methane would behave close to an ideal gas, and thus, would contribute little to the errors in the AR model. The molecular interactions between species also change the phase transition space of mixtures compared to that of the component species. Thus, the AR model will introduce large errors if any of the component species are near the two-phase region. However, if all of the mixture species are sufficiently far away from the phase boundary and critical point, e.g., in the compressed liquid region or ideal gas region, then the AR model and AP model will give equivalent results. For example, AR type models have been successfully used in liquid mixtures of biodiesel-diesel fuels blends [50].

Based on the above results and discussion, it is clear that if the pressures and/or temperatures of the experiment are near one or more of the constituent fluids phase transition point or critical point, the AP model is the only reliable option among the three models. The AP model uses mixture EOS to compute the mixture density but retains the so-called ideal gas behavior to compute the mixture polarizability to yield accurate results. Figure 4 illustrates that (1) computing mixture refractivity as the summation of

mole-weighted refractivity of its components or AR model is grossly inaccurate at high pressures, regardless of the method used to compute the density (ideal gas or real gas), and (2) AP model can accurately predict the refractive index for non-polar binary real gas mixtures. Thus, the higher order terms in Eq. 11b ( $B_1$ ,  $B_2$ , and  $B_{12}$ ) are indeed negligible, especially for the  $CO_2$ - $CH_4$  mixture. Considering that  $CO_2$  exhibited the strongest pressure dependence on pure component polarizability in Fig. 2 (though still  $<5\%$  error), the fact that the AP model accurately captures its mixture behavior with  $CH_4$ , it is expected that the AP model will work for the other combinations of these non-polar substances. The error could be much smaller if the temperature/pressure are farther away from the critical point of one of the components.

Next, Fig. 5 shows comparison of refractive index data for all of the mixtures in Ref [49] with predictions from the AP model. The maximum error is less than  $0.6\%$  indicating robustness of the model. The corresponding maximum error in the computed mole fraction is less than  $3.5\%$ . In summary, the AP model has been demonstrated to accurately predict the refractive index at high pressures with non-ideal gas behavior. A detailed investigation of the possible sources of errors is beyond the scope of this work. However, minor errors observed in Fig. 5 are likely caused by the small effect of pressure on polarizability (see Fig. 2) which are ignored in this study.

## 6. Application Examples

In this section, the models developed above will be applied to investigate fuel-air mixing at compression ignition engine conditions assuming adiabatic

mixing. First, models will be compared against each other for Spray A condition. Next, AP model will be applied for a wide range of engine conditions.

### *6.1. Adiabatic mixing and phase space*

Spray A condition is designed to represent low temperature combustion with moderate exhaust gas recirculation. The fuel for Spray A is *n*-dodecane - a diesel fuel surrogate - injected at a pressure of 1500 bar. The fuel (pre-injection) temperature is 363 K, and the ambient pressure and temperature at the test point are 60 bar and 900 K, respectively. Nitrogen is used as the ambient fluid to limit the discussion to binary mixtures. The fuel temperature changes across the injector, and isenthalpic and isothermal conditions across the injector provide the two limiting bounds for the fuel injection temperature. In this study, the fuel injection temperature is obtained by assuming constant enthalpy across the injector, though this choice only affects specific numbers and not any of the trends or conclusions.

Thermodynamic properties of the mixture are determined by assuming adiabatic fuel-air mixing supported by Siebers and others [51, 52, 53, 54]. Adiabatic mixing assumes: (1) local thermodynamic equilibrium with heat transfer occurring only via mass transfer, i.e., no radiation or exothermic reactions, and (2) non-differential transport of all mass, momentum, and energy, i.e., all Schmidt numbers and Lewis numbers are unity. In turbulent flows, the mixing is dominated by turbulent viscosity transport, which is the basis for most CFD simulations. For example, Ref [53] investigated the effect of a realizable Schmidt number in the near nozzle region and found the results were independent of the Schmidt number. CFD studies have found good agreement with experimental centerline mixing measurements

using adiabatic mixing assumption [54]. Adiabatic mixing assumption will not work in the sooty flame region or even in cool-flame and ignition regimes associated with exothermic reactions.

The time scale for thermodynamic equilibrium are typically much shorter than heat transfer time scales, and mixing assumption is applied locally (each pixel or grid in CFD) to determine the non-uniform mixing behavior. For adiabatic mixing at a constant chamber pressure, fuel enters as liquid at the fuel injection temperature, the ambient gas is at the chamber temperature, and the exiting fluid can be gaseous, liquid, or two-phase mixture. For a given chamber pressure and temperature, the mixture enthalpy and hence, the thermodynamic state of the mixture including its temperature, quality (if two-phase), mixture fraction, and equivalence ratio can be calculated as a function of the fuel mole fraction.

Figure 6 shows mixture temperature versus fuel mole fraction for real gas and ideal gas mixtures. The saturated liquid/vapor lines, two-phase region, and the critical point determined from real-gas EOS for the mixture are also shown. For Spray A fuel injection and ambient conditions, the two-phase mixture occurs at fuel mole fraction of 0.1 (saturated vapor) to 0.9 (saturated liquid). Figure 6 shows that the mixture temperature for ideal and real gas assumptions agree with each other for fuel mole fraction of up to 0.15, but depart significantly at higher fuel mole fractions, i.e., for mixtures in the two-phase region. This result is expected since the ideal gas model assumes a vapor phase for the entire fuel mole fraction (or mixture fraction) space. In the two-phase region, the ideal gas model severely underpredicts the mixture temperature as the fuel mole fraction is increased. The dashed

green line in the two phase region is a spline fit where REFPROP fails to return a valid solution. Note that the two-phase region cannot be quantified by Rayleigh scattering or RSD diagnostics. Thus, reliable measurements can only be obtained in the vapor region, i.e., for fuel mole fraction of up to 0.10 for this test case. Fortunately, this is not a serious drawback for compression ignition engine applications since fuel mole fraction (or equivalence ratio) measurements are needed mainly in the combustible vapor region.

### 6.2. Model Comparison

In this section, the three models (IG, AR, and AP) will be compared at Spray A condition. Model Eqs. 20 will be used to compute the refractive index as a function of fuel mole fraction, which can be related to density, temperature, equivalence ratio, etc. of the mixture. In practice, a look-up table is generated with refractive index as input to determine thermodynamic properties outputs. Figure 7 shows the equivalence ratio and mixture temperature for different models as function of the normalized refractive index difference defined as  $\delta = n/n_0 - 1$  where  $n_0$  is the refractive index of the surrounding ambient - pure nitrogen in this case. The vapor zone (left side,  $\delta < 0.012$ ) and two-phase zone (right side,  $\delta > 0.012$ ) are identified in the figure.

Figure 7 shows that the AR model performs poorly in both vapor and two-phase zones in comparison to the validated AP model. The AR model overpredicts the mixture temperature and slightly underpredicts equivalence ratio even though it uses real-gas properties, again indicating that the additive principle incorporated in the model is grossly inaccurate. This is explained by the chamber conditions being close to the critical point of  $n$ -

dodecane. The IG model performs well in the vapor zone, but it increasingly deviates from the AP model in the two-phase zone. The large deviation in the two-phase region is easy to explain since the IG model treats the two-phase zone as ideal gas as discussed previously. Results show that the IG and AP models are equivalent in the vapor zone, indicating that Spray A can be approximated by the ideal gas assumption. However, one should be aware that the phase boundary must be determined either experimentally or from the real-gas analysis. While a detailed uncertainty analysis is outside the scope of this work, uncertainty in  $\delta$  will propagate to uncertainty in calculated thermodynamic quantities. For example, at Spray A conditions a 1% error in  $\delta$  corresponds to a maximum of a 1% error in  $\phi$  in the vapor region; where the percent error in  $\phi$  decreases as  $\phi$  increases.

### 6.3. Parametric Study

Next, the IG and AR models are compared with the AP model for a wide range of compression ignition engine conditions: Ambient conditions are varied from an assumed engine intake at  $P_{intake} = 2$  bar and  $T_{intake} = 360$  K to top dead center (TDC) at  $P_{TDC} = 200$  bar and  $T_{TDC} = 1250$  K, and the inlet fuel temperature in the chamber is 419 K (after isenthalpically expanding from  $T_{inj} = 363$  K and  $P_{inj} = 1500$  bar). These conditions represent a typical engine with 2 bar boost at the intake and isentropic compression at compression ratio of 6 to 29 to span the range in compression ignition engines. Figures 8 and 9 show, respectively, the absolute error in mixture temperature and equivalence ratio introduced by the IG model when compared to the validated AP model.

The y-axes in Figs. 8,9 represent pairs of chamber (cylinder) pressure

and temperature reached via isentropic compression from the initial state. In Fig. 8, the right edge of the colored region represents  $\phi = 0$  and the left edge is terminated at  $\phi = 50$ . The dashed white line denotes the phase boundary with vapor on the right and two-phase region on the left side. Figure 8 shows that the IG model does quite well in the vapor zone (<5% error). i.e., the IG model is adequate in the vapor zone for most diesel applications. However, one could inadvertently apply the IG model in the two-phase region causing large errors ( $\approx 20\%$  error). If the IG model is used, the two-phase boundary must be identified from either real-gas analysis or diagnostics for liquid boundary detection. Such errors can be avoided by applying the AP model throughout the operational regime.

Figure 9 shows the error in the equivalence ratio introduced by the IG model. The right side of the colored region represents the phase boundary. Figure 9 shows that the IG model introduces larger errors at higher compression ratios (or high chamber temperatures and pressures). Figure 9 identifies region with errors above 5% (solid white line) and 10 % (dashed white line). However, for pressures below 100 bar, the error in equivalence ratio is small indicating that the IG model is adequate.

Next, Fig. 10 shows the error in mixture temperature and equivalence ratio introduced by the AR model as compared to the validated AP model. Even in the vapor zone, the temperature is overpredicted or underpredicted by as much as 150 C. At low chamber pressures (or temperatures), the error is greater near the phase boundary, but at high pressures, it is confined to fuel-lean conditions with significant compressibility effects. Figure 11 further supports the poor performance of the AR model. Even in the vapor zone,

the errors in equivalence ratio could be up to 80%. As such, the AR model should not be used in optical diagnostics of gas mixtures at high pressures.

#### 6.4. *Supercritical Fuel-Oxidizer Mixing*

The AP model will reach its full potential at conditions departing from the ideal gas behavior, e.g., transcritical and supercritical mixing regimes. Recent experimental and theoretical findings have stimulated interest in supercritical fuel-oxidizer mixing at diesel conditions. [12, 13, 14, 15, 16, 17, 18]. Thus, the ability to acquire quantitative thermodynamic measurements in the supercritical regime is of great interest. However, purely supercritical mixing in diesel engines requires either much higher ambient pressures (and thus, temperatures) or fuel modifications, e.g., high injection temperature or fuels with low critical temperature. In this study, propane at Spray A conditions is used to simulate supercritical mixing. Figure 12 shows that the mixture temperature for propane at supply temperature of 395 K (after isenthalpically expanding from  $T_{inj} = 363$  K and  $P_{inj} = 1500$  bar), i.e., slightly above its critical temperature of 370 K, injected into an ambient at Spray A conditions (60 bar and 900 K) never enters the two-phase regime and thus completely diffusive mixing without surface tension (or no droplets) is likely to occur. Absence of droplets could potentially allow RSD or Rayleigh scattering measurements across the entire mixture fraction space.

Figure 13 shows equivalence ratio and mixture temperature versus refractive index difference (or fuel mole fraction) for the three models presented in this study. For refractive index difference,  $\delta$ , less than 0.01, all three models provide similar results indicating that the mixture is close to an ideal gas. For refractive index difference of 0.02 or fuel mole fraction of 0.5, the mixture

temperature is underpredicted by about 25°C by the IG model and overpredicted by about 25°C by the AR model. For fuel mole fraction greater than 0.5 ( $\delta > 0.02$ ), the IG model is no longer useful since it deviates exponentially from the accurate AP model. The AR model is also inaccurate for fuel mole fractions between 0.5 and 0.96. The poor performance of the IG model can be attributed to the significant compressibility effects in this fully supercritical mixing regime. The AR model approaches the AP model at fuel mole fraction close to unity when the mixture approaches a pure substance. However, the AP model would be the method of choice to accurately calculate both mixture temperature and equivalence ratio across the entirety of the mixture fraction space for mixing at purely supercritical conditions.

## 7. Conclusions

This study investigated the effect of pressure on polarizability and density to extend the Lorentz-Lorenz equation to real-gas mixtures at high pressure. Three different formulations of the Lorentz-Lorenz equation for gaseous mixtures were compared against experimental data in the literature. The Additive Polarizability (AP) model was identified as the robust model for applications at the harshest conditions. The AP model was validated using published experimental data on refractive index and then used to estimate errors in the other two models (IG and AR models) for a wide range of compression ignition engine operating conditions. Finally, the AP model was applied to study supercritical mixing of propane and nitrogen. Following is a summary of the conclusions from this study:

- The original Lorentz-Lorenz equation should be used instead of the sim-

plified Dale-Gladstone equation to eliminate unwarranted errors that can affect the thermophysical property calculations.

- For liquids, both polarizability and density are nearly constant. However, for non-polar gases, the polarizability is nearly constant while density varies significantly with pressure. In contrast, density variation with pressure is linear in the ideal-gas regime, but highly non-linear near the critical point and phase change boundaries of component species and mixture.
- Following the additive principle (e.g., Amagat law), the mixture laws for Lorentz-Lorentz equation can be expressed as mole weighted sum of component refractivity (product of polarizability and density) or polarizability. For incompressible liquids (constant density) or ideal gases (linear variation in density with pressure), both formulations yield the same result. However, they are different when density varies non-linearly with pressure, for example, near the critical point and/or phase boundaries of components or mixture.
- In the ideal-gas regime, the IG, AR, and AP models are equivalent. In the compressed liquid region where density is linear with mixture fraction, the AR and AP models are equivalent.
- In the non-linear density regime, the IG and AR models can be highly inaccurate. The AR model performs poorly across the entire range of compression ignition conditions, yielding errors in equivalence ratio of up to 80%.

- The AP model works well across the entire compression ignition engine regimes including conditions near the critical point and phase boundaries. The IG model is valid in the vapor region (assuming it is known) at the typical compression ignition engine operating conditions. However, IG model could introduce large errors if inadvertently applied to the two-phase region, for example, in CFD analysis.

## 8. Acknowledgements

This work was performed with support by the Department of Energy, Office of Energy Efficiency and Renewable Energy (EERE) and the Department of Defense, Tank and Automotive Research, Development, and Engineering Center (TARDEC), under Award Number DE-EE0007301.

## 9. References

### References

- [1] C. Espey, J. E. Dec, T. A. Litzinger, D. A. Santavicca, Planar laser rayleigh scattering for quantitative vapor-fuel imaging in a diesel jet, *Combustion and flame* 109 (1997) 65–86.
- [2] C. A. Idicheria, L. M. Pickett, Quantitative mixing measurements in a vaporizing diesel spray by Rayleigh imaging, Technical Report, SAE Technical Paper, 2007.
- [3] A. Adam, P. Leick, G. Bittlinger, C. Schulz, Visualization of the evaporation of a diesel spray using combined mie and rayleigh scattering techniques, *Experiments in fluids* 47 (2009) 439–449.

- [4] R. B. Miles, W. R. Lempert, J. N. Forkey, Laser rayleigh scattering, *Measurement Science and Technology* 12 (2001) R33.
- [5] F.-Q. Zhao, H. Hiroyasu, The applications of laser rayleigh scattering to combustion diagnostics, *Progress in energy and combustion science* 19 (1993) 447–485.
- [6] L. Pickett, G. Bruneaux, R. Payri, Engine combustion network, Sandia National Laboratories, Livermore, CA, <http://www.ca.sandia.gov/ecn> (2014).
- [7] A. K. Agrawal, C. T. Wanstall, Rainbow schlieren deflectometry for scalar measurements in fluid flows, *Journal of Flow Visualization and Image Processing* 25 (2018).
- [8] C. T. Wanstall, A. K. Agrawal, J. A. Bittle, Quantifying liquid boundary and vapor distributions in a fuel spray by rainbow schlieren deflectometry, *Applied optics* 56 (2017) 8385–8393.
- [9] C. T. Wanstall, A. K. Agrawal, J. A. Bittle, Phase boundary detection in transient, evaporating high-pressure fuel sprays by rainbow schlieren deflectometry, *Applied Optics* (2019).
- [10] B. W. Albers, A. K. Agrawal, Schlieren analysis of an oscillating gas-jet diffusion flame, *Combustion and flame* 119 (1999) 84–94.
- [11] W. Meier, R. S. Barlow, Y.-L. Chen, J.-Y. Chen, Raman/rayleigh/lif measurements in a turbulent  $\text{CH}_4/\text{H}_2/\text{N}_2$  jet diffusion flame: experimental techniques and turbulence–chemistry interaction, *Combustion and Flame* 123 (2000) 326–343.

- [12] R. N. Dahms, J. Manin, L. M. Pickett, J. C. Oefelein, Understanding high-pressure gas-liquid interface phenomena in diesel engines, *Proceedings of the Combustion Institute* 34 (2013) 1667–1675.
- [13] R. N. Dahms, J. C. Oefelein, On the transition between two-phase and single-phase interface dynamics in multicomponent fluids at supercritical pressures, *Physics of Fluids* 25 (2013) 092103.
- [14] R. N. Dahms, J. C. Oefelein, Non-equilibrium gas–liquid interface dynamics in high-pressure liquid injection systems, *Proceedings of the Combustion Institute* 35 (2015) 1587–1594.
- [15] R. N. Dahms, Understanding the breakdown of classic two-phase theory and spray atomization at engine-relevant conditions, *Physics of Fluids* 28 (2016) 042108.
- [16] Z. Falgout, M. Rahm, Z. Wang, M. Linne, Evidence for supercritical mixing layers in the ecn spray a, *Proceedings of the Combustion Institute* 35 (2015) 1579–1586.
- [17] Z. Falgout, M. Rahm, D. Sedarsky, M. Linne, Gas/fuel jet interfaces under high pressures and temperatures, *Fuel* 168 (2016) 14–21.
- [18] C. Crua, J. Manin, L. M. Pickett, On the transcritical mixing of fuels at diesel engine conditions, *Fuel* 208 (2017) 535–548.
- [19] R. N. Dahms, J. C. Oefelein, Liquid jet breakup regimes at supercritical pressures, *Combustion and Flame* 162 (2015) 3648–3657.

- [20] H. Lee, A. Fernandez-Pello, G. Corcos, A. Oppenheim, A mixing and deformation mechanism for a supercritical fuel droplet, *Combustion and Flame* 81 (1990) 50–58.
- [21] J. Shuen, V. Yang, C. Hsiao, Combustion of liquid-fuel droplets in supercritical conditions, *Combustion and Flame* 89 (1992) 299–319.
- [22] J. Oefelein, R. Dahms, G. Lacaze, Detailed modeling and simulation of high-pressure fuel injection processes in diesel engines, *SAE International Journal of Engines* 5 (2012) 1410–1419.
- [23] J. Oefelein, G. Lacaze, R. Dahms, A. Ruiz, A. Misdariis, Effects of real-fluid thermodynamics on high-pressure fuel injection processes, *SAE International Journal of Engines* 7 (2014) 1125–1136.
- [24] G. Lacaze, A. Misdariis, A. Ruiz, J. C. Oefelein, Analysis of high-pressure diesel fuel injection processes using les with real-fluid thermodynamics and transport, *Proceedings of the Combustion Institute* 35 (2015) 1603–1611.
- [25] X. Wang, H. Huo, U. Unnikrishnan, V. Yang, A systematic approach to high-fidelity modeling and efficient simulation of supercritical fluid mixing and combustion, *Combustion and Flame* 195 (2018) 203–215.
- [26] D. Aspnes, Local-field effects and effective-medium theory: a microscopic perspective, *American Journal of Physics* 50 (1982) 704–709.
- [27] H. A. Lorentz, *The Theory of Electrons and Its Applications to the Phenomena of Light and Radiant Heat: A Course of Lectures Delivered*

- in Columbia University, New York in March and April, 1906, volume 29, Teubner, 1916.
- [28] W. Gardiner Jr, Y. Hidaka, T. Tanzawa, Refractivity of combustion gases, *Combustion and Flame* 40 (1981) 213–219.
- [29] R. Bosque, J. Sales, Polarizabilities of solvents from the chemical composition, *Journal of chemical information and computer sciences* 42 (2002) 1154–1163.
- [30] H. Achtermann, G. Magnus, T. Bose, Refractivity virial coefficients of gaseous  $\text{CH}_4$ ,  $\text{C}_2\text{H}_4$ ,  $\text{C}_2\text{H}_6$ ,  $\text{CO}_2$ ,  $\text{SF}_6$ ,  $\text{H}_2$ ,  $\text{N}_2$ ,  $\text{He}$ , and  $\text{Ar}$ , *The Journal of chemical physics* 94 (1991) 5669–5684.
- [31] J. W. Schmidt, M. R. Moldover, Dielectric permittivity of eight gases measured with cross capacitors, *International Journal of Thermophysics* 24 (2003) 375–403.
- [32] A. H. Harvey, E. W. Lemmon, Method for estimating the dielectric constant of natural gas mixtures, *International journal of thermophysics* 26 (2005) 31–46.
- [33] A. Buckingham, J. Pople, The dielectric constant of an imperfect non-polar gas, *Transactions of the Faraday Society* 51 (1955) 1029–1035.
- [34] A. Buckingham, The molecular refraction of an imperfect gas, *Transactions of the Faraday Society* 52 (1956) 747–753.
- [35] A. Buckingham, J. Pople, Electromagnetic properties of compressed gases, *Discussions of the Faraday Society* 22 (1956) 17–21.

- [36] A. Buckingham, R. Raab, The dielectric constant of a compressed gas mixture, *Transactions of the Faraday Society* 54 (1958) 623–628.
- [37] D. L. Goldfarb, D. P. Fernández, H. R. Corti, Dielectric and volumetric properties of supercritical carbon dioxide (1)+ methanol (2) mixtures at 323.15 k, *Fluid phase equilibria* 158 (1999) 1011–1019.
- [38] Y. Sun, B. Y. Shekunov, P. York, Refractive index of supercritical co 2-ethanol solvents, *Chemical Engineering Communications* 190 (2003) 1–14.
- [39] R. Span, *Multiparameter equations of state: an accurate source of thermodynamic property data*, Springer Science & Business Media, 2013.
- [40] W. C. Reynolds, P. Colonna, *Thermodynamics*, Cambridge University Press, 2018.
- [41] E. W. Lemmon, R. T. Jacobsen, A new functional form and new fitting techniques for equations of state with application to pentafluoroethane (hfc-125), *Journal of Physical and Chemical Reference Data* 34 (2005) 69–108.
- [42] E. W. Lemmon, R. Jacobsen, A generalized model for the thermodynamic properties of mixtures, *International journal of thermophysics* 20 (1999) 825–835.
- [43] E. W. Lemmon, R. Tillner-Roth, A helmholtz energy equation of state for calculating the thermodynamic properties of fluid mixtures, *Fluid phase equilibria* 165 (1999) 1–21.

- [44] I. H. Bell, E. W. Lemmon, Automatic fitting of binary interaction parameters for multi-fluid helmholtz-energy-explicit mixture models, *Journal of Chemical & Engineering Data* 61 (2016) 3752–3760.
- [45] E. Lemmon, M. Huber, M. McLinden, Refprop 9.1, NIST standard reference database 23 (2013).
- [46] Y. Liu, P. H. Daum, Relationship of refractive index to mass density and self-consistency of mixing rules for multicomponent mixtures like ambient aerosols, *Journal of Aerosol Science* 39 (2008) 974–986.
- [47] F. Croccolo, M.-A. Arnaud, D. Bégué, H. Bataller, Concentration dependent refractive index of a binary mixture at high pressure, *The Journal of chemical physics* 135 (2011) 034901.
- [48] M. V. Avdeev, A. N. Konovalov, V. N. Bagratashvili, V. K. Popov, S. I. Tsykina, M. Sokolova, J. Ke, M. Poliakoff, The fibre optic reflectometer: A new and simple probe for refractive index and phase separation measurements in gases, liquids and supercritical fluids, *Physical Chemistry Chemical Physics* 6 (2004) 1258–1263.
- [49] C. Giraudet, L. Marlin, D. Bégué, F. Croccolo, H. Bataller, Concentration dependent refractive index of co<sub>2</sub>/ch<sub>4</sub> mixture in gaseous and supercritical phase, *The Journal of Chemical Physics* 144 (2016) 134304.
- [50] S. Geacai, I. Nita, O. Iulian, E. Geacai, Refractive indices for biodiesel mixtures, *UPB Sci. Bull. Ser. B* 74 (2012) 149–160.
- [51] D. L. Siebers, Liquid-phase fuel penetration in diesel sprays, *SAE transactions* (1998) 1205–1227.

- [52] D. L. Siebers, Scaling liquid-phase fuel penetration in diesel sprays based on mixing-limited vaporization, Technical Report, SAE technical paper, 1999.
- [53] J. Desantes, J. M. García-Oliver, J. Pastor, A. Pandal, E. Baldwin, D. Schmidt, Coupled/decoupled spray simulation comparison of the ecn spray a condition with the  $\sigma$ -y eulerian atomization model, *International Journal of Multiphase Flow* 80 (2016) 89–99.
- [54] J. M. Garcia-Oliver, J. M. Pastor, A. Pandal, N. Trask, E. Baldwin, D. P. Schmidt, Diesel spray cfd simulations based on the  $\sigma$ -y eulerian atomization model, *Atomization and Sprays* 23 (2013) 71–95.

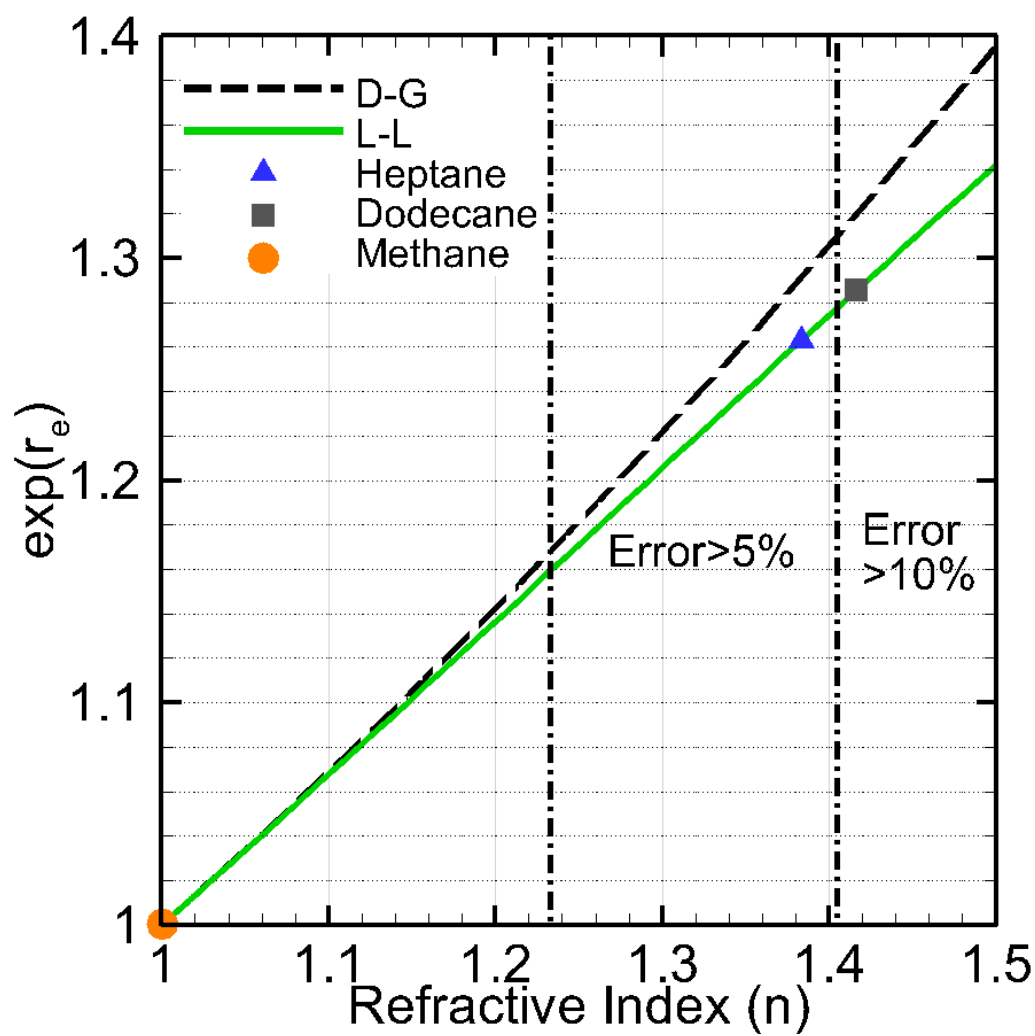


Figure 1: A plot showing the exponential of refractivity ( $r_e$ ) based on the Lorentz-Lorenz (L-L) equation and the Dale-Gladstone (D-G) approximation for three different fuels.

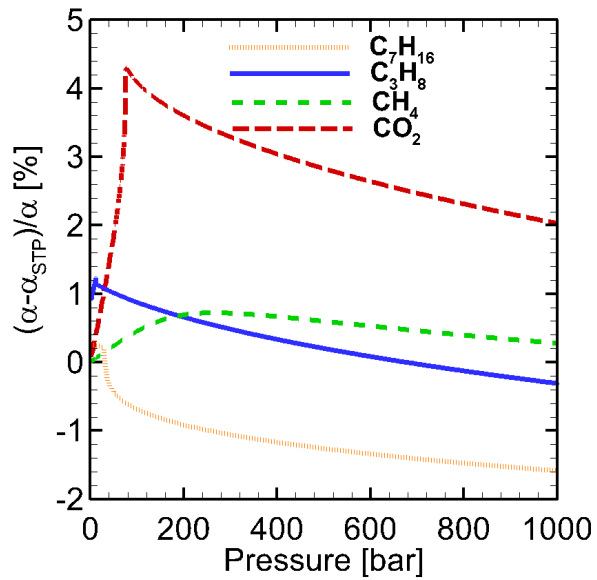
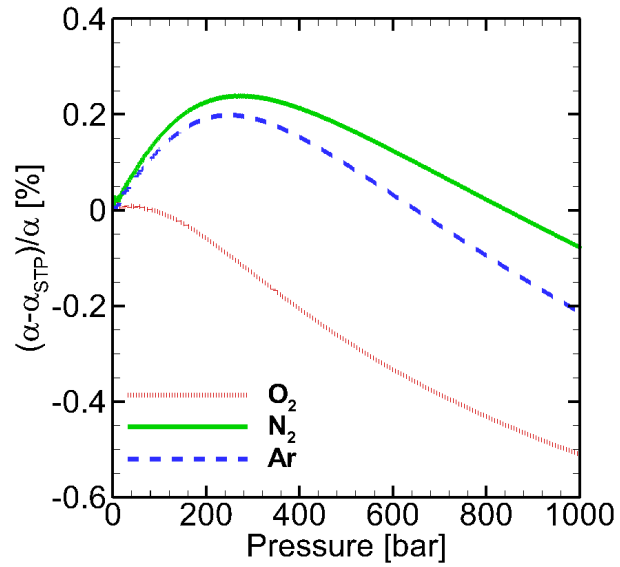


Figure 2: Effect of pressure on polarizability of constituents of air (top) and hydrocarbons and carbon dioxide (bottom). The vertical axis shows the percent change in polarizability with respect to the value at STP (273 K and 1 bar) except 550 K and 1 bar for n-heptane.

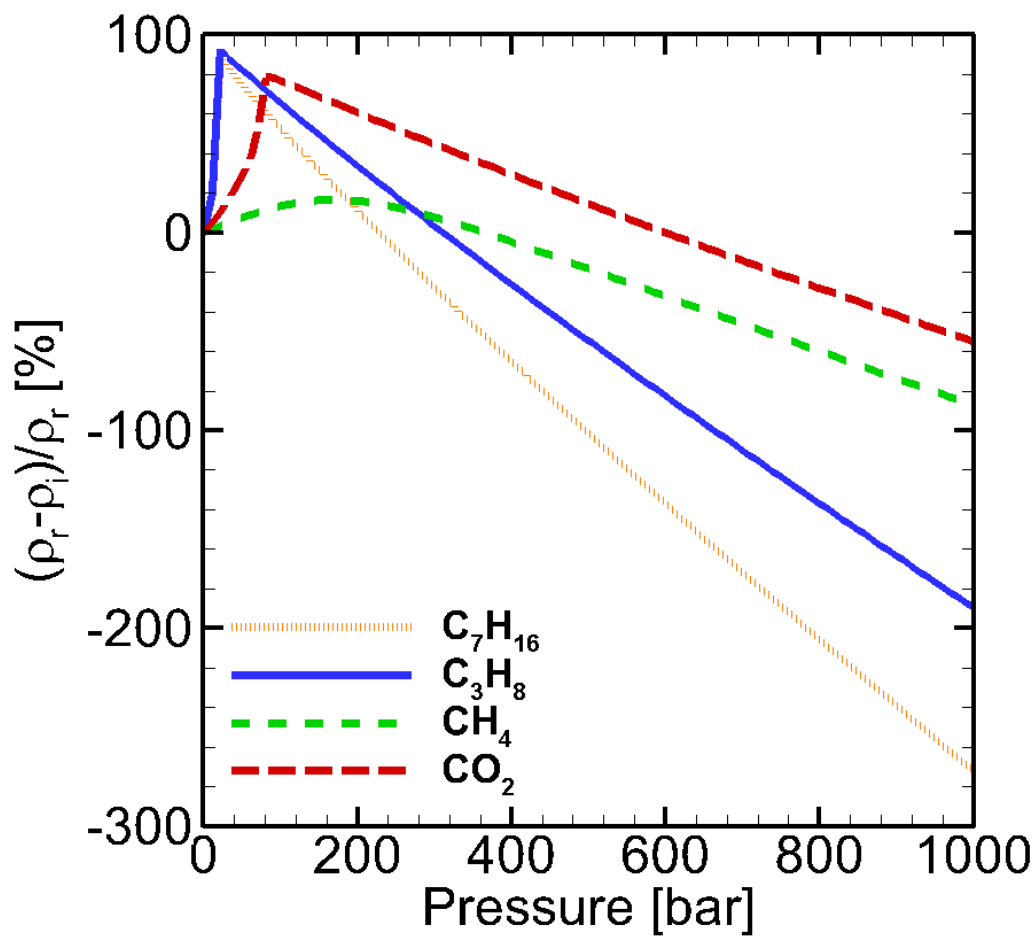


Figure 3: Effect of pressure on density for hydrocarbons and carbon dioxide. The vertical axis shows the percent difference in density computed by real-gas and ideal gas models. Reference conditions are STP (273 K and 1 bar) except 550 K and 1 bar for n-heptane.

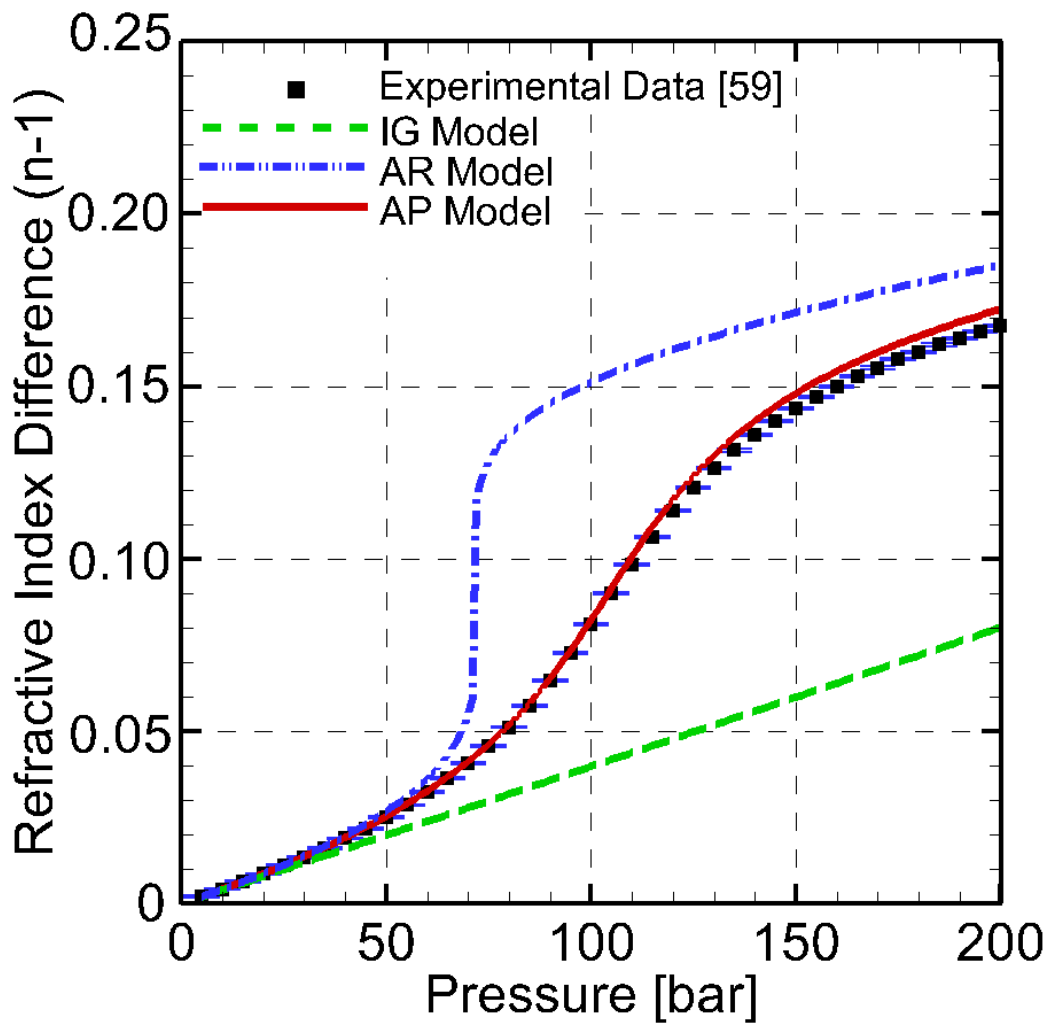


Figure 4: Refractive index difference versus pressure for a binary mixture of 78.2% CO<sub>2</sub> 21.8% CH<sub>4</sub> at a temperature of 303 K.

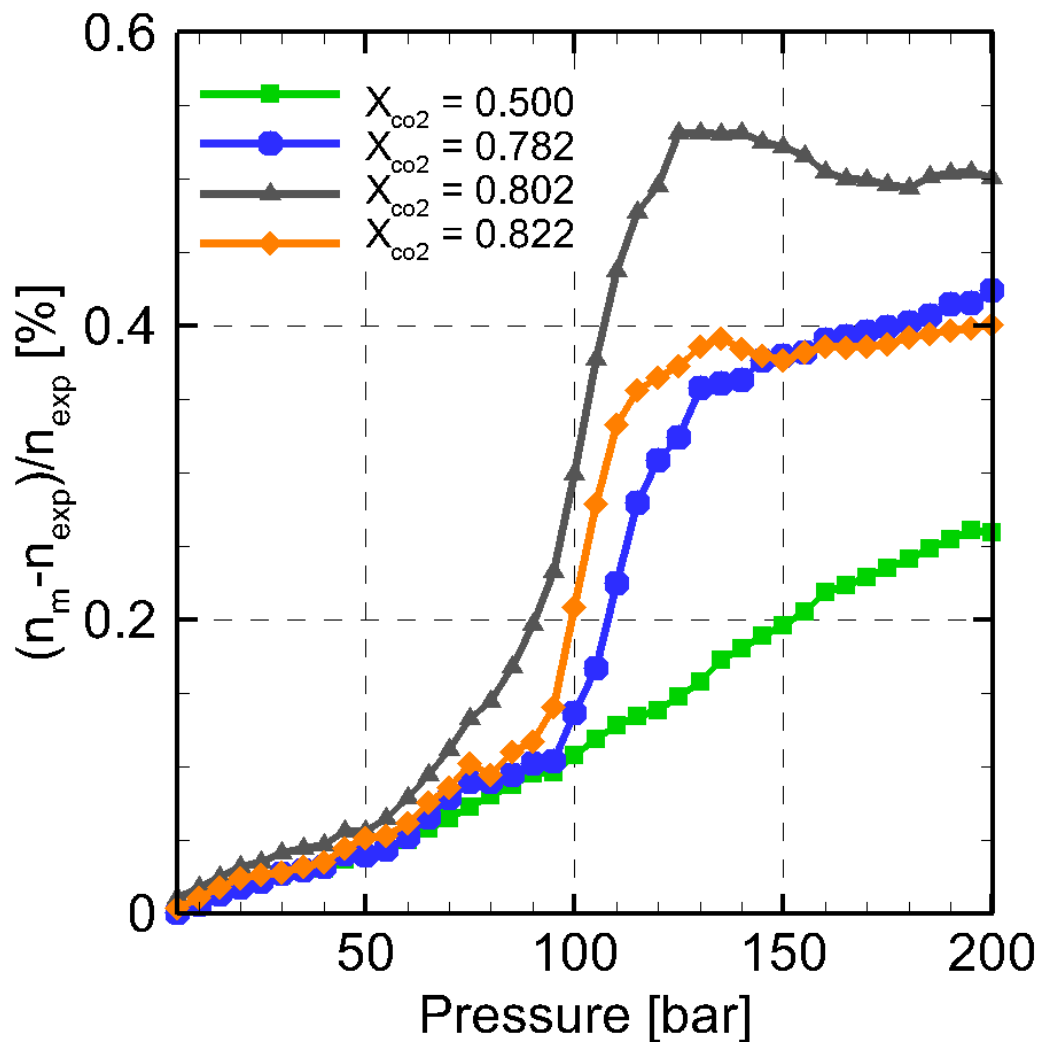


Figure 5: Percent difference in predicted (by the AP model) and experimental refractive index data of Ref. [49] at a temperature of 303 [K].

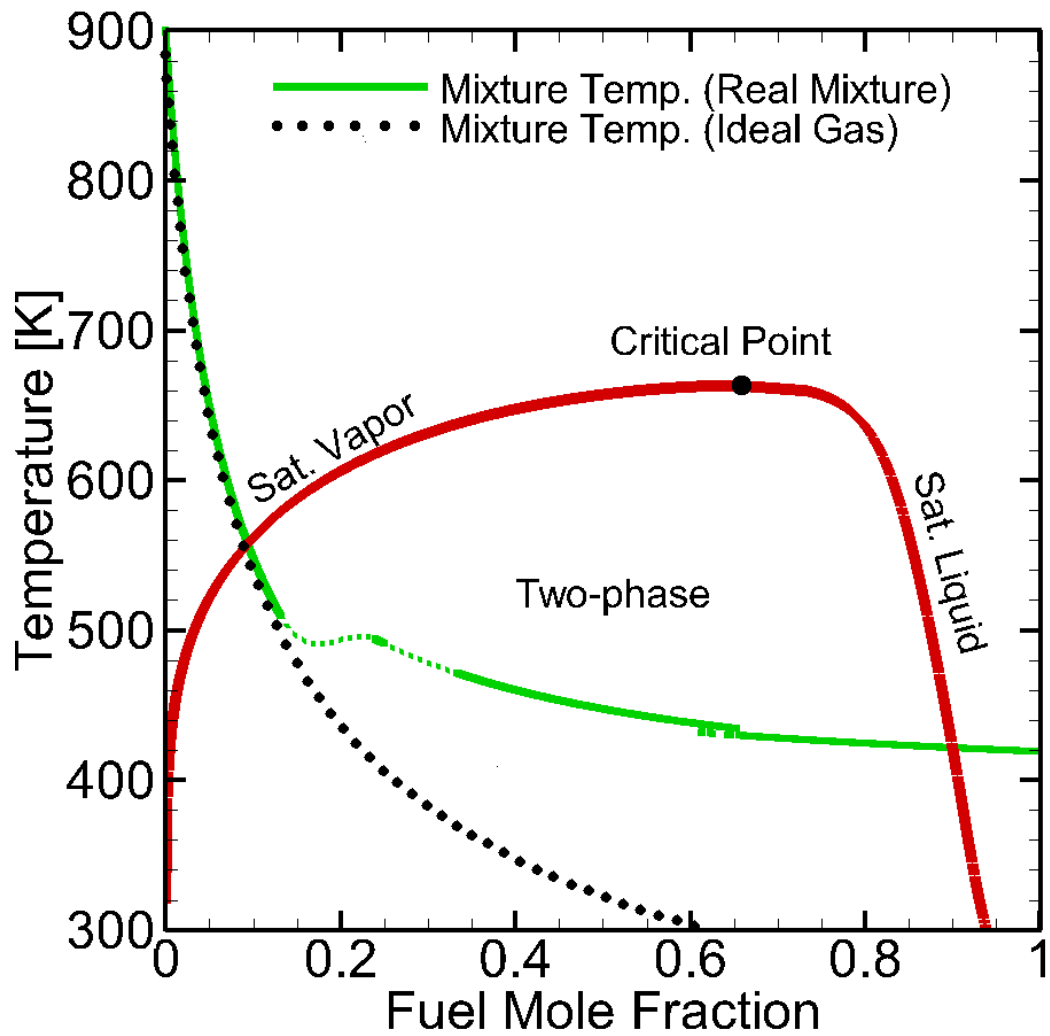


Figure 6: Temperature vs fuel mole fraction binary mixture of *n*-dodecane and nitrogen at Spray A conditions. The phase boundaries and vapor-liquid equilibrium region are also shown.

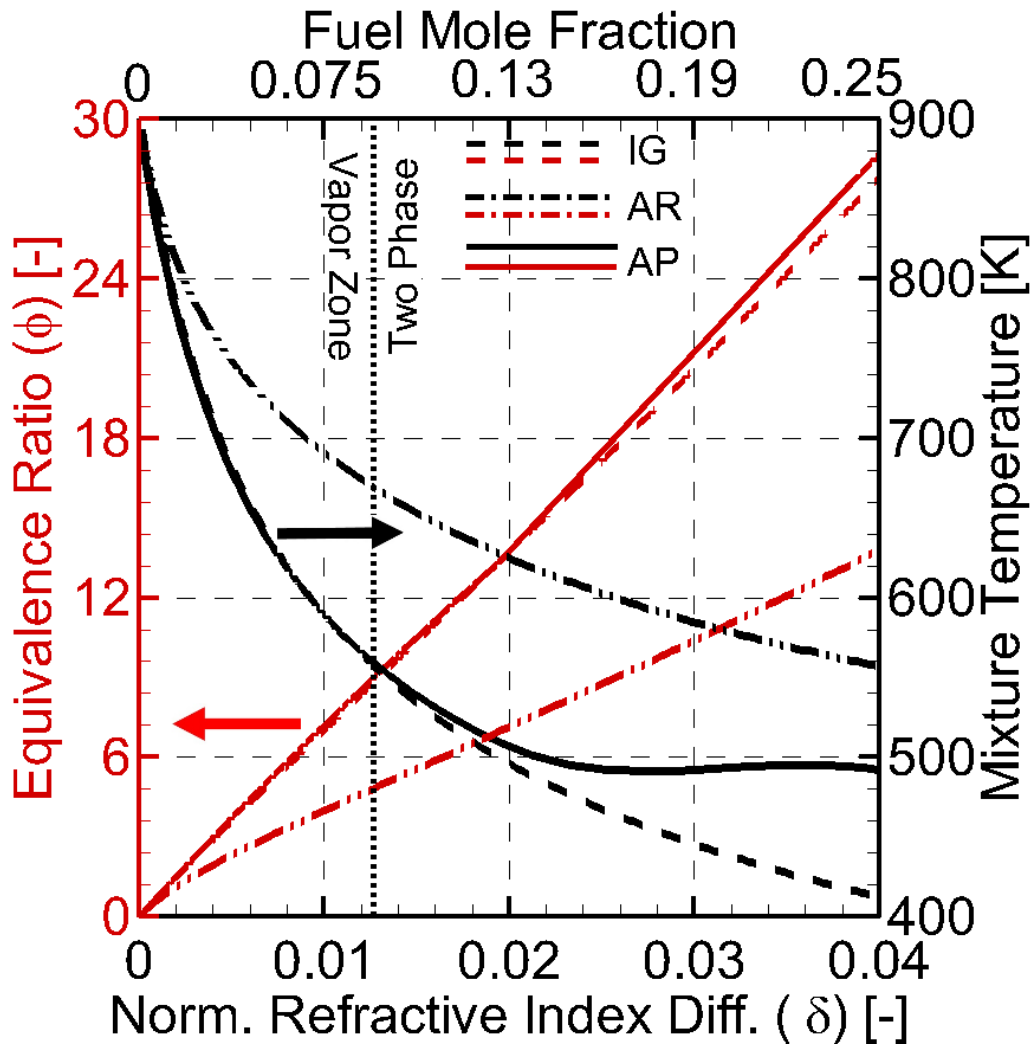


Figure 7: Equivalence ratio and mixture temperature as function of normalized refractive index difference for the IG, AR, and AP models.

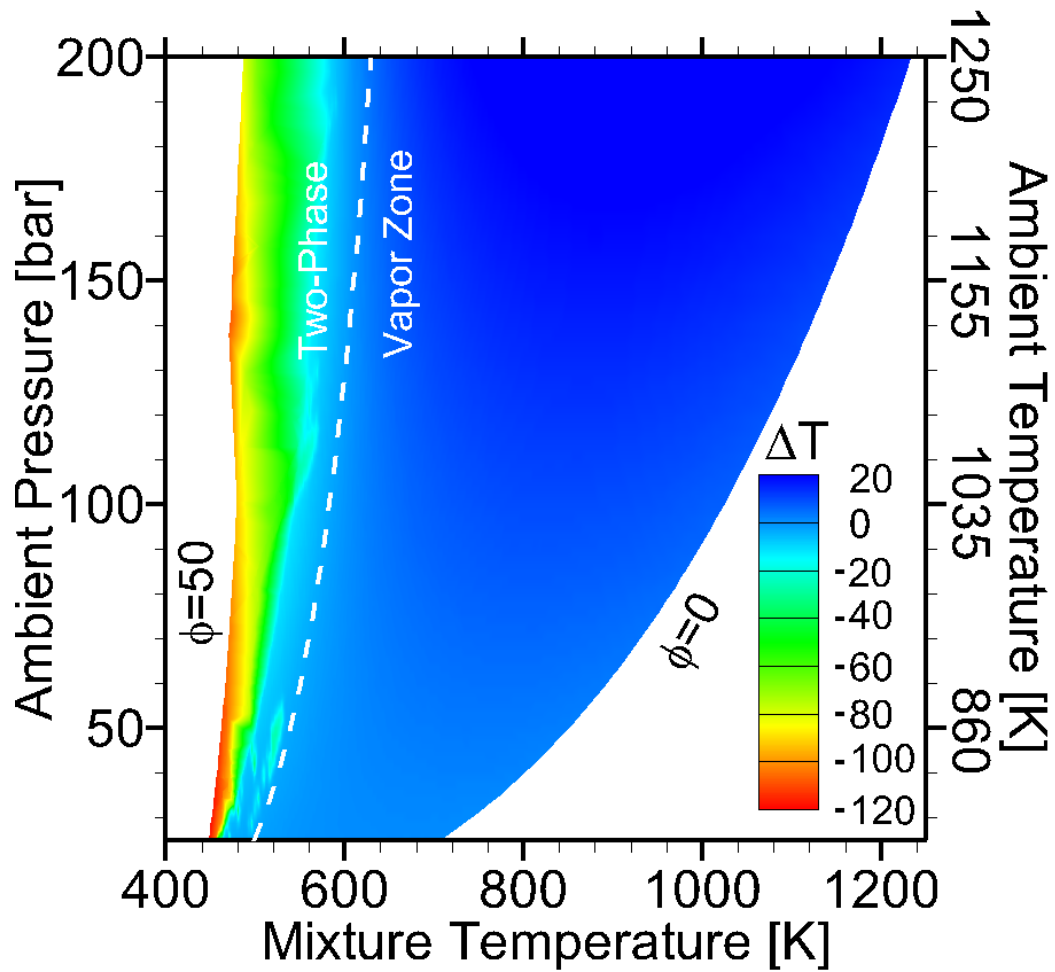


Figure 8: Absolute error in the mixture temperature calculated using the IG model ( $\Delta T = T_{IG} - T_{AP}$ ) for *n*-dodecane and nitrogen as a function of ambient conditions (pairs for pressure and temperature assuming isentropic compression from  $P_i = 2$  bar  $T_i = 360$  K). The dashed white line represents the two-phase boundary.

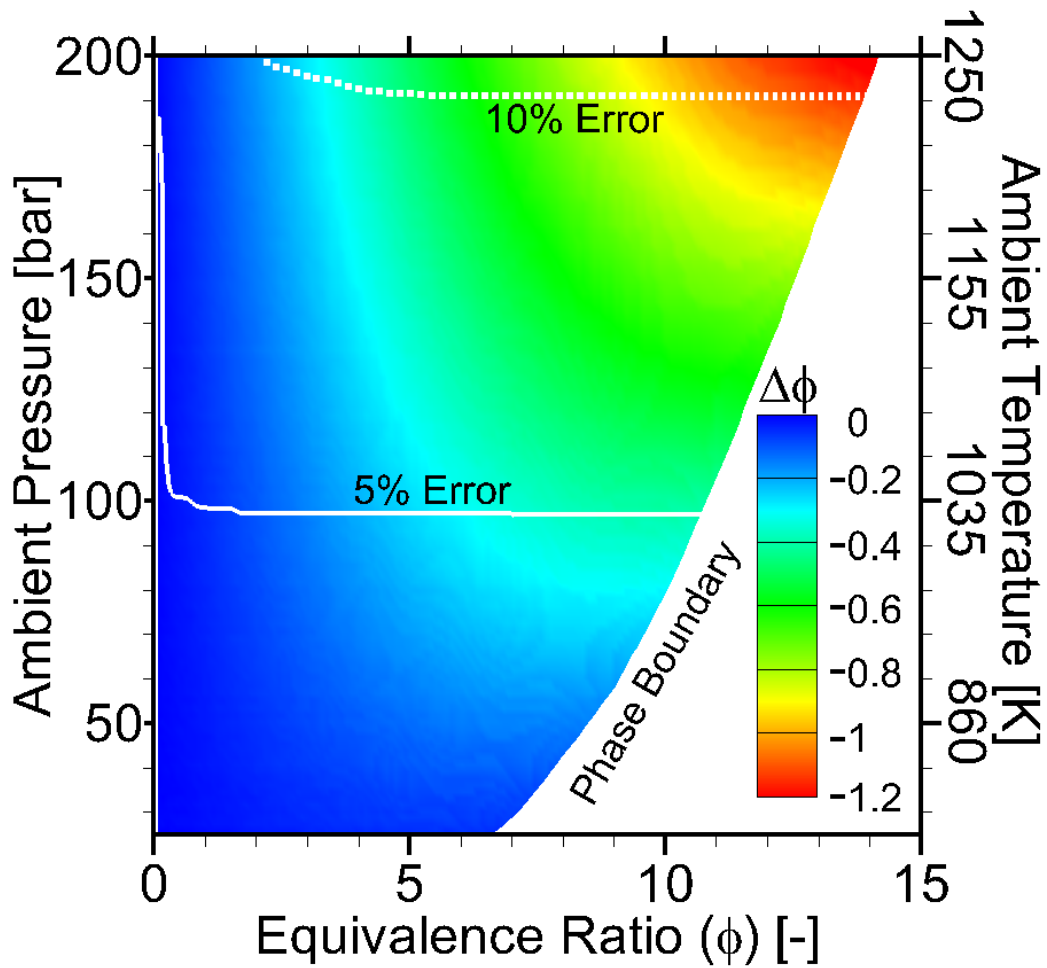


Figure 9: Absolute error in the equivalence ratio calculated using the IG model ( $\Delta\phi = \phi_{IG} - \phi_{AP}$ ) for *n*-dodecane and nitrogen as a function of ambient conditions (pairs for pressure and temperature assuming isentropic compression from  $P_i = 2$  bar  $T_i = 360$  K) for gas phase mixtures. The solid and dashed white lines are error isolines of 5% and 10%, respectively.

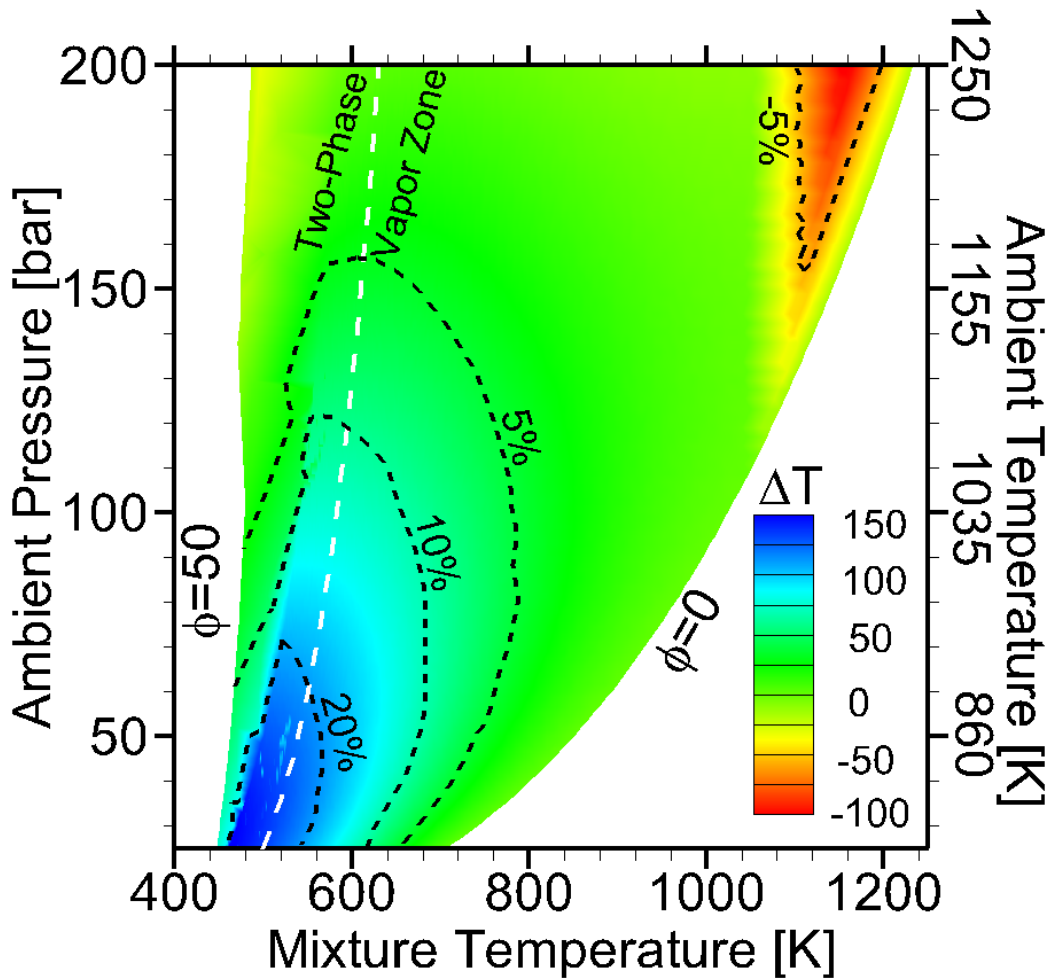


Figure 10: Absolute error in the mixture temperature calculated using the AR model ( $\Delta T = T_{AR} - T_{AP}$ ) for *n*-dodecane and nitrogen as a function of ambient conditions (pairs for pressure and temperature assuming isentropic compression from  $P_i = 2$  bar  $T_i = 360$  K). The dashed white line represents the two-phase boundary and the black dashed lines represent percent error isolines.

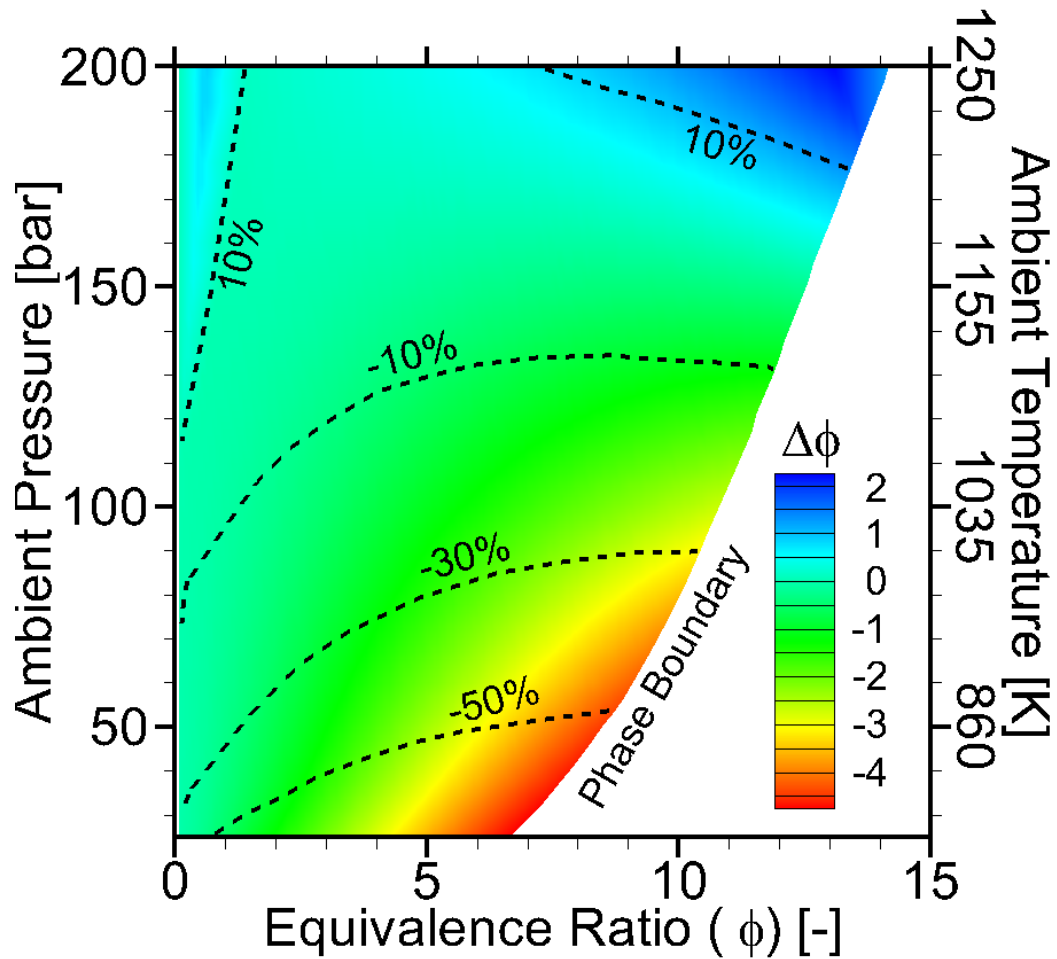


Figure 11: Absolute error in equivalence ratio is calculated using the AP and AR model ( $\Delta\phi = \phi_{AR} - \phi_{AP}$ ) for *n*-dodecane and nitrogen as a function of ambient conditions (pairs for pressure and temperature assuming isentropic compression from  $P_i = 2$  bar  $T_i = 360$  K) for gas phase mixtures. The right edge of the contour represents the phase boundary. Percent error isolines are overlaid as black dashed lines.

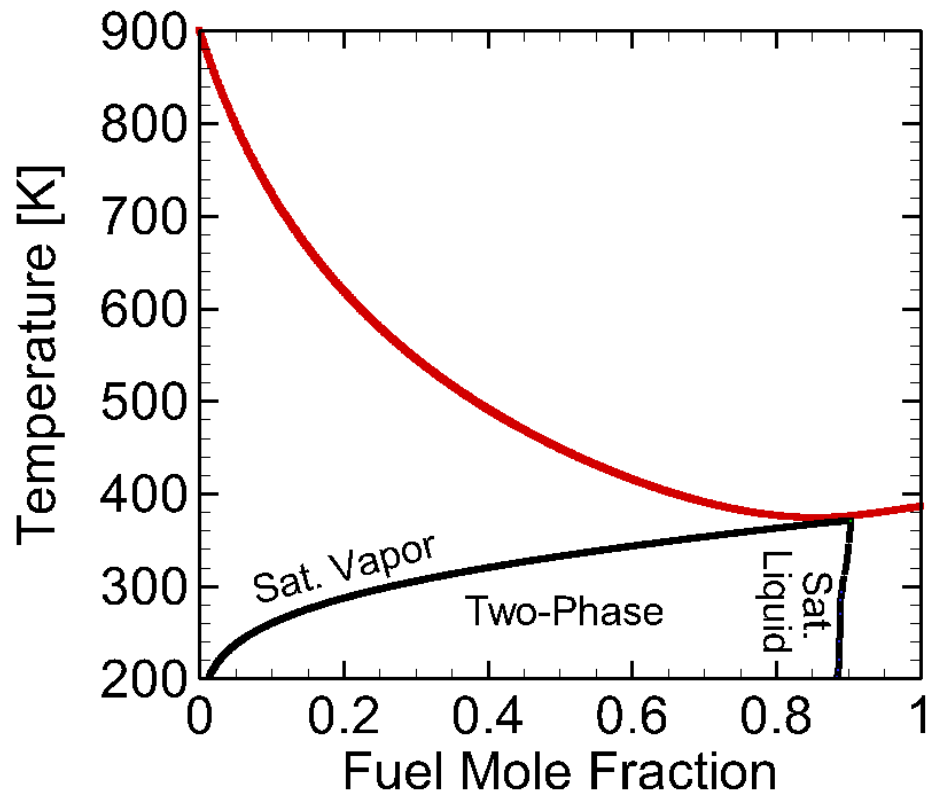


Figure 12: Calculated temperature versus fuel mole fraction for binary propane-nitrogen mixture at Spray A conditions using the IG, AR, and AP models.

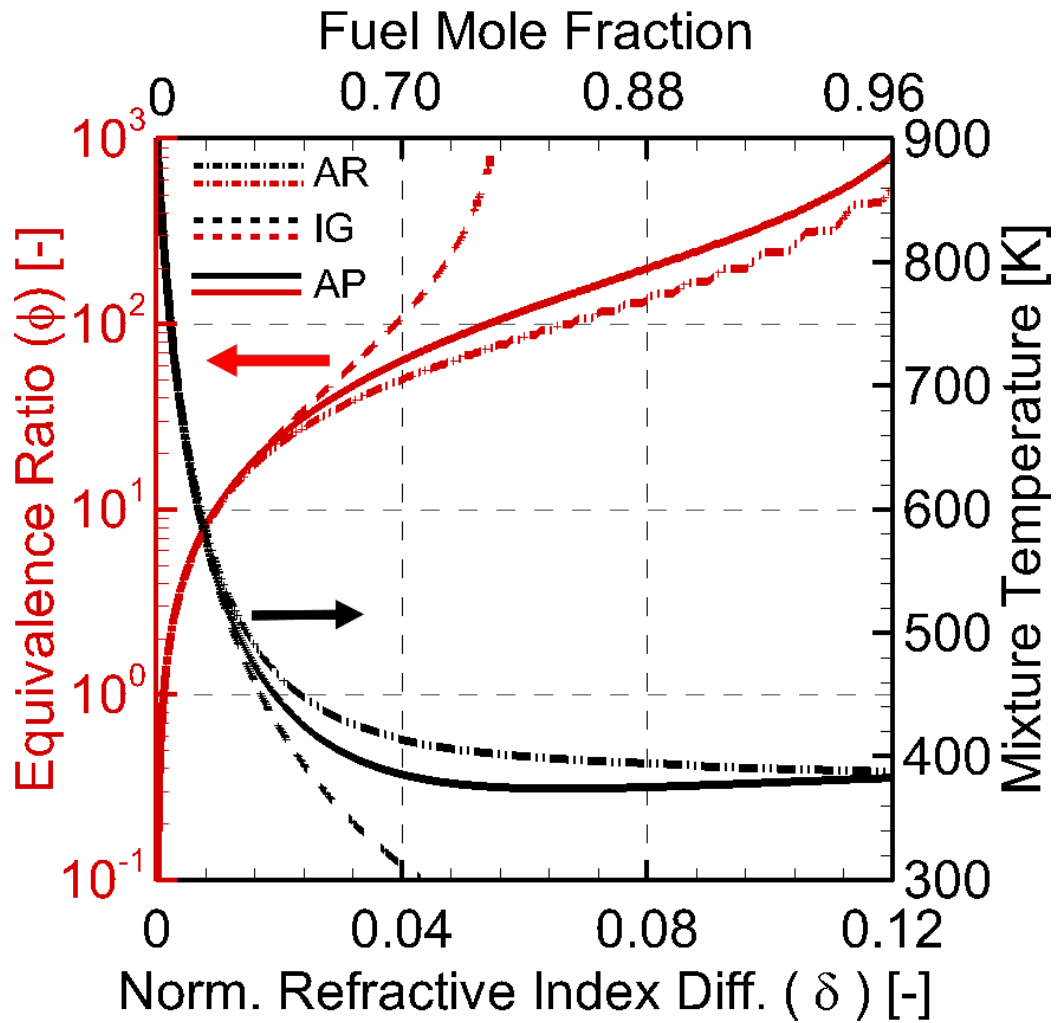


Figure 13: Equivalence ratio and mixture temperature as function of normalized refractive index difference for binary propane-nitrogen mixture at Spray A conditions calculated using the IG, AR, and AP models.